THE JOURNAL OF PHYSICAL CHEMISTRY C

Article

Cite This: J. Phys. Chem. C 2018, 122, 23528−23542

pubs.acs.org/JPCC

# Methane Adsorption and Self-Diffusion in Shale Kerogen and Slit Nanopores by Molecular Simulations

Stéphane Tesson[†,‡] and Abbas Firoozabadi*[,†]

[†]Reservoir Engineering Research Institute, 595 Lytton Avenue, Suite B, Palo Alto, California 94301, United States

[‡]Department of Chemical and Environmental Engineering, University of California Riverside, Riverside, California 92521, United States

Supporting Information

**ABSTRACT:** Shale gas has redefined the energy landscape in the world. The scientific community makes efforts to exploit shale gas resources with minimum environmental impact. Shale gas is mainly located in micropores and mesopores of shale rocks. Molecular simulations provide insights into the kerogen structure frameworks and hydrocarbon and nonhydrocarbon adsorption on the kerogen-accessible surface. In this work, a new method is introduced to create kerogen slit nanopores from the molecular scale with different surface roughness. The hybrid molecular dynamics-grand canonical Monte Carlo (MD-GCMC) simulations are used to investigate methane adsorption in a rigid and flexible kerogen matrix and slit nanopores at three different temperatures and various pressures. Molecular dynamics simulations are used to study $CH_4$ mobility in the flexible kerogen matrix and slit nanopores. Our simulation results show that the kerogen matrix is a dynamic system in which a coupling may exist between gas adsorption and kerogen matrix structure deformation. The chemical composition and flexibility of kerogen molecules affect adsorption and self-diffusion in the kerogen matrix. Surface roughness and chemical composition have a significant effect on adsorption in the kerogen slit nanopores. The effect of kerogen molecular flexibility on self-diffusion in slit nanopores may not be significant. Our work is based on type II-A kerogen macromolecules, but our methodology for creating kerogen slit nanopores can be used for other types of kerogen molecules.

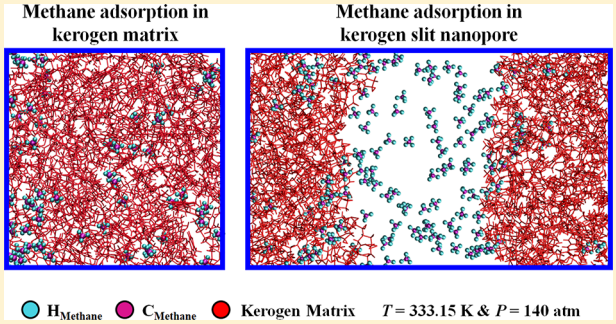


## INTRODUCTION

Shale gas has redefined the energy landscape.[1,2] In the U.S., shale formations currently provide about 40% of the total natural gas production. In 2035, it may rise to more than 45%.[3] In China, there is rapid expansion in shale gas production; the current production is about 148 billion cubic meters per year.[4] In 2018, China's natural gas production may rise by 9% over 2017.[5] Scientific efforts are being made to exploit shale gas resources[6] with minimum environmental impact.[7,8]

Shale gas is mainly located in micropores (pore diameter between 10 and 20 Å) and mesopores[9,10] (pore diameter between 20 and 500 Å). Shale rocks consist of inorganic minerals (quartz, clays, calcites, etc.) and organic matter (kerogens and bitumens). The organic matter is mainly composed of kerogen, and it is considered as the main methane trapping. Kerogen is insoluble in common polar solvents, such as chloroform and dichloromethane.[11] Its physicochemical properties depend on the origin and on the burial history.[12,13] Four different kerogen types[14−16] can be distinguished: (i) type I from a lacustrine anoxic environment, (ii) type II from marine shale and continental planktons, (iii) type III from plants in tertiary and quaternary coals, and (iv) type IV from older sediments redeposited after erosion. All types can be classified according to the van Krevelen diagrams,[11,17,18] based on the elemental ratios of hydrogen/carbon (H/C), oxygen/carbon (O/C), and sulfur/carbon (S/C).

In a subsurface environment, kerogen is exposed to several environmental constraints (temperature, pressure, fluids, etc.). Under these conditions the type of kerogen plays a significant role in the microstructure of the kerogen matrix (porosity and surface shape of the pores) and in fluid behavior confined in kerogen pores. The link between mechanical deformation and gas adsorption may be a key process in shale gas production; this interplay remains unsolved. Fluids can be in the adsorbed state on the rock surface, as free molecules in the pores, and as dissolved molecules in the kerogen matrix.[19] Adsorption on the surfaces may provide a significant share of fluid-in-place. The identification of adsorption mechanism at various conditions is crucial with respect to the determination of kerogen physicochemical−mechanical behavior. The adsorption is mostly associated with the accessible surface area and adsorbate content. Most of the experimental research has focused on adsorption in shale samples,[20−26] but recent studies report adsorption of methane, carbon dioxide, and light hydrocarbons

Received: July 24, 2018
Revised: September 21, 2018
Published: September 26, 2018






DOI: 10.1021/acs.jpcc.8b07123
J. Phys. Chem. C 2018, 122, 23528−23542

(propane, *n*-butane, and iso-butane) in isolated kerogen.[26−29] Experimental studies on the kerogen microstructure deformations remain a challenge.

Molecular simulations provide insights into the kerogen structure frameworks, adsorption, and transport. Several molecular simulations have been made to investigate the kerogen matrix properties.[13,18,30−44] Most authors[13,31,33−42,44] use Ungerer's methodology[11] to create the kerogen matrix. In this approach, first, kerogen macromolecules are placed in a large simulation box. Then, the system is brought to realistic density by successive molecular dynamics (MD) simulations that result in equilibration of the system. Some authors[18,30,32,43] have created the kerogen matrix by using a hybrid reverse Monte Carlo reconstruction technique. In the construction of the system's configuration, the kerogen microstructure is not imposed.[13,38−40,42] The use of dummy particles (DPs)[31,34,37,45,46] and specific molecules[47] (such as $CO_2$, $H_2O$, hydrocarbons, etc.) allows control of microstructure.

The structure of the pores affects gas adsorption in kerogen. Vasileiadis et al.[37] investigated by MD simulations the structure of the kerogen matrix based on 15, 50, and 100 type II-D kerogen macromolecules at $T$ = 298.15 K and $P$ = 1 atm. The porosity of the kerogen matrix was imposed by the number (0, 1, 2, or 3) and the size of dummy particles ($\sigma_{DP}$ = 15, 20, 30, and 40 Å). They found that the methane-accessible surface area increased with increasing the number of kerogen macromolecules, the number of DPs, and the size of DPs. Huang et al.[42] characterized by MD simulations the structure of the kerogen matrix based on 12 type II-D kerogen macromolecules (without DP and specific molecules) at $T$ = 300 K and $P$ = 1 bar. They reported a helium-accessible surface area of 1764 $m^2\ g^{-1}$. Sui and Yao[13] studied by MD simulations the structure of the kerogen matrix based on 6 type II-A kerogen macromolecules (without DP and specific molecules) at $T$ = 300 K and $P$ = 1 MPa. They reported a methane-accessible surface area of 1548 $m^2\ g^{-1}$. Collell et al.[47] created a kerogen matrix based on 4 type II-C kerogen macromolecules and 2 molecules of asphaltenes/resins at $T$ = 300 K and $P$ = 20 MPa. They found a methane-accessible surface area of 86 ± 10 $m^2\ g^{-1}$. The accessible surface area is related to the kerogen maturity, the number of kerogen macromolecules (or kerogen fragments), and the method used to create pores.

Gas adsorption has been investigated by molecular simulations at different temperature and pressure conditions in different kerogen matrices. Huang et al.[42] performed GCMC simulations of methane adsorption in four different rigid kerogen matrices based on (1) 6 type II-A kerogen macromolecules, (2) 7 type II-B kerogen macromolecules, (3) 7 type II-C kerogen macromolecules, and (4) 12 type II-D kerogen macromolecules at $T$ = 318 K and pressures to 18 MPa. Methane adsorptions were, respectively, ∼0.6 mmol $g^{-1}$, ∼0.8 mmol $g^{-1}$, ∼1 mmol $g^{-1}$, and ∼2.8 mmol $g^{-1}$ for the kerogen matrix 1, 2, 3, and 4 at 18 MPa. Zhao et al.[39] performed GCMC simulations for methane adsorption in three different rigid kerogen matrices based on (1) 12 immature kerogen macromolecules, (2) 11 oil window mature kerogen macromolecules, and (3) 10 post-mature kerogen macromolecules at $T$ = 298, 323, and 348 K and pressures to 15 MPa. They found the same methane adsorption trend as in Huang et al.[42] Zhao et al.[39] and Sui and Yao[13] performed GCMC simulations to compute methane adsorption in the rigid kerogen matrix at $T$ = 298 K and $P$ to 15 MPa. The kerogen matrix was created based on 10 (Zhao et al.[39]) and 6 (Sui and Yao[13]) type II-A kerogen macromolecules. They calculated methane adsorption of 1.22 mmol $g^{-1}$ (Zhao et al.[39]) and 3.2 mmol $g^{-1}$ (Sui and Yao[13]). Zhao et al.[40] and Huang et al.[42] performed GCMC simulations to compute methane adsorption in the rigid kerogen matrix at $T$ = 298 and 318 K and $P$ to 18 MPa. The kerogen matrix was created based on 11 (Zhao et al.[40]) and 12 (Huang et al.[42]) type II-D kerogen macromolecules. They found methane adsorption of 3.7 mmol $g^{-1}$ (Zhao et al.[40]) and 2.8 mmol $g^{-1}$ (Huang et al.[42]). Recently, Vasileiadis et al.[44] performed GCMC simulations to compute adsorption of $CH_4$, $C_2H_6$, *n*-$C_4H_{10}$, $CO_2$, and their mixtures in the rigid kerogen matrix described above at 298.15 and 398.15 K and pressures to 250 atm. They justified the use of a rigid kerogen matrix by the fact that methane adsorption was very close in the rigid and flexible kerogen matrix. They computed a methane adsorption of 0.06 mmol $g^{-1}$ and 0.065 mmol $g^{-1}$ at 1 atm and 398.15 K in the rigid and flexible kerogen matrix, respectively. At 20 atm and 298.15 K, they calculated methane adsorption of 1.91 mmol $g^{-1}$ and 1.93 mmol $g^{-1}$ in the rigid and flexible kerogen matrix, respectively. The conclusion of the authors is that adsorption may not be affected by the flexibility of kerogen molecules at low pressure. In this work we will investigate the effect of pressure on flexibility of kerogen molecules to 400 atm which is higher than the past work. We will then show as pressure increases the adsorption becomes more pronounced. In a recent paper, Ho et al.[41] have shown that the flexibility of the kerogen matrix and the simulation box affect adsorption due to a chemo-mechanical coupling between gas adsorption and medium deformation. They investigated methane adsorption in the flexible kerogen matrix based on 27 type II-A kerogen macromolecules in a flexible simulation box at $T$ = 300 K and $P$ to 192 atm. Ho et al.[41] found that methane adsorption was ∼1.5 times higher in the flexible kerogen matrix (∼4 mmol $g^{-1}$) than in the rigid kerogen (∼2.6 mmol $g^{-1}$) at $P$ = 192 atm. The increase in adsorption is related to the microstructure change and the type of the kerogen matter. One of the objectives of this investigation is further study of flexible kerogen molecules on adsorption to a pressure of 400 atm.

The diffusion of hydrocarbons in kerogen is important in shale gas transport. Collell et al.[47] have investigated the self-diffusion coefficient of light hydrocarbons: $CH_4$, $C_2H_6$, $C_3H_8$, *n*-$C_4H_{10}$, and *n*-$C_8H_{18}$ in kerogen media at $T$ = 300 K and $P$ = 20 MPa. They found that the diffusivity decreased with the increase of molecular weight from 4.8 ± 1.4 [$10^{-9}$ $m^2\ s^{-1}$] ($CH_4$) to 2.4 ± 1.4 [$10^{-9}$ $m^2\ s^{-1}$] (*n*-$C_8H_{18}$). The self-diffusion coefficient of light hydrocarbons in the kerogen matrix is lower by an order of magnitude in comparison to bulk. Vasileiadis et al.[44] calculated the diffusivity of two light hydrocarbons: $CH_4$ and $C_2H_6$ in kerogen matrix at 298.15 and 398.15 K at various pressures. They found that methane diffused ∼2 times faster than $C_2H_6$, and the diffusivity increased with increasing temperature. Wang et al.[38] investigated the self-diffusion coefficient of $CH_4$ and $CO_2$ mixture in type II-A kerogen media at 333.15 K at various pressures. They found that due to the anisotropy of the kerogen structure, the self-diffusion coefficients of methane and carbon dioxide were different in different directions and decrease gradually with the increase of pressure.

Adsorption, diffusion, and transport have been also investigated in slit nanopores which is a model for more complex nanoporous media.[48−52] The comparison is then made on surface area equivalency as well as pore size and slit nanopore widths. Most adsorption studies are made in carbon slit nanopores of smooth surfaces. Wu et al.[50] investigated by MD simulations the adsorption and transport of methane in carbon slit nanopores at 298 K at pressures to 16 MPa. They presented



DOI: 10.1021/acs.jpcc.8b07123
J. Phys. Chem. C 2018, 122, 23528−23542

the change in the structure of methane adsorbed layers with the slit pore width increase. At low pressure, the smallest slit pore fills up quickly and stores more methane than the largest slits. Jin and Firoozabadi[51,52] studied by GCMC simulations methane adsorption in carbon slit nanopores of varying widths at room temperature and different pressures. They showed that methane-adsorbed layers decrease as the slit pore width increases. These conditions do not take into account the kerogen physicochemical properties, surface chemistry, and surface roughness. Simulations in the smooth slit nanopore may not represent the behavior in kerogen or shale media as we will demonstrate in this paper.

Recently, slit nanopores based on kerogen fragments[53,54] and kerogen macromolecules[55] have been introduced. Different methods have been used to create kerogen slit nanopores. Sun et al.[53] placed different mature kerogen fragments in two large simulation boxes and performed MD simulations to create two kerogen matrices. Then, they put both kerogen matrices in the same simulation box, separated by an empty space of 21 Å to build a kerogen slit nanopore fixing all the atomic positions. The kerogen slit nanopore had smooth surfaces. Zhang et al.[54] placed more than 100 different mature kerogen fragments in one large simulation box and performed MD simulations to create the kerogen matrix. Then, the kerogen slit nanopore was created by deleting atoms and bonds for a 20, 50, and 100 Å slit thickness. They fixed all the atomic positions. The kerogen slit nanopore had smooth surfaces. Okamoto et al.[55] used a kerogen slit nanopore, with very rough surfaces, based on type III kerogen macromolecules, and a quartz slit nanopore with a smooth surface. They fixed all the atomic positions. They did not discuss the method used to create the kerogen slit nanopore.

Adsorption and diffusion in kerogen slit nanopores may depend on the surface chemistry and its surface roughness. Sun et al.[53] investigated by GCMC simulations adsorption of methane, carbon dioxide, and their mixture in the rigid kerogen slit nanopore described above at four different temperatures (298, 323, 343, and 373 K) to a pressure of 20 000 kPa. They did not observe well-defined adsorption peaks and found that adsorption increases with pressure and decreases with temperature. They showed that methane self-diffusion decreased from the center of the kerogen slit nanopore to the kerogen matrix inside. This decrease is due to the surface roughness and the surface chemistry of the slit nanopore and to the adsorbate confinement inside small pores of the kerogen matrix. The system by these authors does not represent the structural properties of kerogen macromolecules, and the use of a rigid structure does not allow the fluid molecules to move through the kerogen matrix. Zhang et al.[54] studied methane adsorption by GCMC simulations in the rigid kerogen slit nanopores described above at different temperatures ($T$ = 333 and 363 K) and pressures (1−25 MPa). Because of the method used to create the kerogen slit nanopore, they observed two well-defined adsorption peaks. They found that methane distribution was affected by the pore width. The average gas density in the 2 nm kerogen slit nanopore was higher than in 5 and 10 nm slits. They also observed that methane adsorption on pore surfaces is not even. They related this observation to the surface chemistry (interactions between different kerogen atoms and methane molecules), the roughness of kerogen nanopores, and the pore morphology. Okamoto et al.[55] investigated by MD simulations methane adsorption in the rigid slit nanopores described above with a wide range of pore widths at 300 K and 12 MPa. They noted that the dynamics of adsorbates were not well-known for nanopore systems because of the complexity from pore size, surface chemistry, surface roughness, wettability, etc. They found that the density of the adsorbed phase was higher in the quartz slit nanopore surfaces than in the kerogen slit nanopore with rough surfaces. They observed two well-defined adsorption peaks on the quartz slit nanopore surfaces and mildly sharp adsorption peaks in the kerogen slit nanopore surfaces. Moreover, they found that the effect of roughness becomes significant in very small kerogen nanopores (less than 6 nm). One may conclude that gas adsorption is intimately related to the surface chemistry and the roughness of the slit nanopore surfaces. To the best of our knowledge, the effect of varying surface roughness of the kerogen slit nanopores on gas adsorption has not been studied. The flexibility of kerogen molecules comprising the slit nanopore and associated flexible kerogen matrix on gas diffusivity has not been also investigated. The objectives of this work are to gain insights into both topics.

This study aims to investigate and to compare methane adsorption and self-diffusion in kerogen slit nanopores and the kerogen matrix based on molecular simulations of flexible macromolecules. A combination of MD and GCMC simulations is used. The manuscript is organized as follows. First, the kerogen macromolecule and the computational details of the simulation methods are provided. Then, the creation of the kerogen matrix and slit nanopores is presented. Next, we investigate the kerogen microstructures and methane adsorption and self-diffusion both in the kerogen matrix and in the slit nanopores. At the end we draw conclusions.

## MATERIALS AND METHODS

**Kerogen Model.** Our investigation is centered on adsorption and self-diffusion in type II kerogen medium, which is the most common source of shale gas.[20,36−58] Type II kerogen is rich in hydrogen and low in carbon, and it can also be rich in sulfur.[14,17] Four different type II kerogens are distinguished according to the stage of maturation: immature (type II-A), top of oil window (type II-B), middle−end of oil window (type II-C), and overmature (type II-D).[15,59,60] We selected the type II-A kerogen macromolecule proposed by Ungerer et al.[11] The elemental ratios are close to the isolated kerogen samples studied in our laboratory.[28,29,61] The chemical formula and molecular mass are, respectively, $C_{252}H_{294}O_{24}N_6S_3$ and 3887.3 g mol$^{-1}$. The structure is presented in Figure 1. The physicochemical properties are listed in Table S1 in the Supporting Information (SI).

**Simulation Methods.** Molecular dynamics simulations are performed in the NVT and NPT ensemble in order to create a kerogen matrix and kerogen slit nanopores. In the NVT ensemble we study methane ($CH_4$; $q_{\text{Carbon CH}_4}$ = −0.2120 e; $q_{\text{Hydrogen CH}_4}$ = +0.0530 e) mobility in the flexible kerogen matrix and flexible kerogen slit nanopores. The LAMMPS[62] software (version 31st March 2017) is used. The time steps in MD simulations in the NVT and NPT ensemble are, respectively, 1.0 and 0.1 fs. These time steps are short enough to capture the carbon−hydrogen bond vibration. The periodic boundary conditions (PBCs) are used in the three directions of space. The temperature and the pressure are, respectively, controlled via the Nosé−Hoover thermostat[63,64] and barostat[65,66] with a relaxation time of 1 ps. The polymer consistent force field plus (PCFF+)[67−70] is used for kerogen, graphite, and methane. The total potential is composed of two terms:

$$V_{\text{Total}} = V_{\text{Bonded}} + V_{\text{Nonbonded}} \quad (1)$$

The first term ($V_{\text{Bonded}}$) represents the bonding interactions, which include the bond length, bond angle, dihedral, improper,



DOI: 10.1021/acs.jpcc.8b07123
J. Phys. Chem. C 2018, 122, 23528−23542

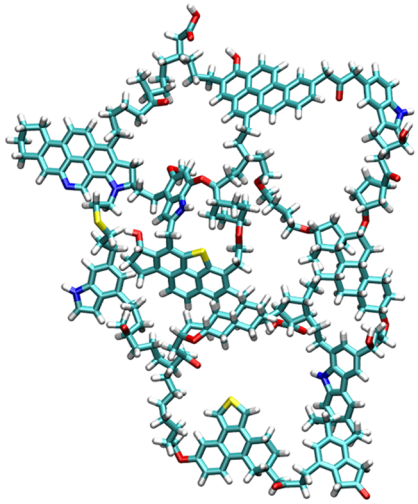


**Figure 1.** Type II-A kerogen macromolecule.[11]

and cross-term potentials. The second term ($V_{\text{Nonbonded}}$) accounts for the nonbonding interactions between atomic pairs: 9-6 Lennard-Jones (LJ) potential and Coulombic potential. Lennard-Jones interactions are calculated with a cutoff distance of 9.5 Å, and the LJ cross terms are derived from the Wäldman and Hagler combining rules.[71] Electrostatic interactions are computed using the Ewald summation.

A hybrid Monte Carlo (MC) method based on molecular dynamics and grand canonical Monte Carlo[72] (MD-GCMC) is used to perform simulations in order to investigate methane absolute adsorption in a rigid and flexible kerogen matrix (KM) and rigid slit nanopores (SPs). MD-GCMC simulations are performed with the same software as the MD simulations. A GCMC cycle including 100 GCMC exchanges (addition and deletion are each attempted with 50% probability) and 100 GCMC moves (translation and rotation are each attempted with 50% probability) was performed after every 100 MD steps. MD simulations are carried out in the NVT ensemble during 2 ns using a time step of 0.1 fs. The temperature is controlled via the Nosé–Hoover thermostat[63,64] with a relaxation time of 1 ps, and the same force field as for the MD simulations is used. The MD simulations allow for a more thorough search of configuration space. The simulations were run on a 32- or 48-core Dell workstation.

**System Characterization.** Porosity, accessible surface, the largest pore size, and pore size distribution (PSD) are investigated by the MC algorithms. Porosity and accessible surface area are calculated by probe particles: nitrogen molecule ($\sigma_{N_2}$ = 3.653 Å) and methane molecule ($\sigma_{CH_4}$ = 3.752 Å) simplified by a single sphere (Figure 2). The results for $CH_4$ and $N_2$ are expected to be similar because the molecular diameters are close.

Porosity was computed by the Herrera et al.[73] method. The principle consists of inserting random probe particles inside the simulation box. The criterion of this method is based on the distance between the center of mass of the probe particle and those of the kerogen's atoms

$$D_{ij} \geq R_i + R_j \tag{2}$$

where $D_{ij}$, $R_i$, and $R_j$ are, respectively, the distance between the center of mass of the probe particle $i$ and the center of mass of the nearest kerogen atom $j$, the radius of the probe particle, and the radius of the kerogen atom. If the probe particle does not overlap with the kerogen atoms, the insertion is accepted. Porosity is the ratio of accepted insertions ($N_{\text{Acc}}$) to the total number of insertions ($N_{\text{Tot}}$)

$$V_{\text{Porosity}}\ [\%] = \frac{N_{\text{Acc}}}{N_{\text{Tot}}} \times 100 \tag{3}$$

Accessible surface area was computed by the Düren et al.[74] method. The principle consists of rolling a probe particle at the surface of the pores of the kerogen matrix to determine the accessible surface area.

The largest pore size and PSD were calculated by the method proposed by Bhattacharya and Gubbins.[75] The principle of this method is based on inserting random particles inside the simulation box, increasing the size of the inset particles and determining the largest sphere from the center of mass of the probe particle. The criterion of the method is based on the distance

$$R_i \leq D_{ij} - R_j \tag{4}$$

and the particle should not overlap with any of the kerogen's atoms.

The microscopic self-diffusion of methane was calculated from the Einstein equation[38,47,76] based on the mean-squared displacement (MSD). The MSD is defined as

$$\Delta\mathbf{r}^2(t) = \langle|\mathbf{r}(t) - \mathbf{r}(0)|^2\rangle \tag{5}$$

where $\mathbf{r}(0)$ and $\mathbf{r}(t)$ are, respectively, the initial position and the position at time $t$. From the Einstein equation, the diffusion coefficient is defined as

$$D_{\text{Dif}} = \frac{\Delta\mathbf{r}^2(t)}{t \times 2 \times d} \tag{6}$$

where $D_{\text{Dif}}$ is the diffusion coefficient, $d$ the dimension of the diffusion coefficient ($d$ = 1, 2, 3), and $t$ the simulation time. In this work, the dimension of the diffusion coefficient is three.

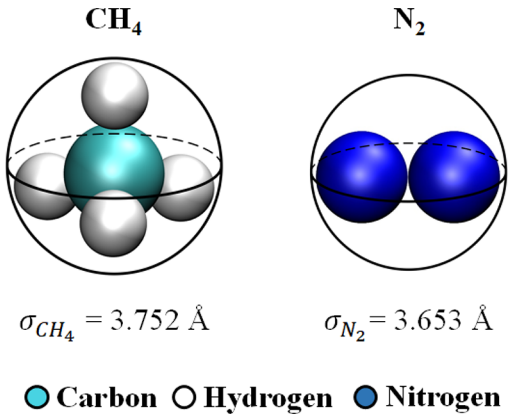


**Figure 2.** Methane and nitrogen probe particles.

## SYSTEM CREATION

**Kerogen Matrix.** First, the force field parameters of each atom of the type II-A kerogen macromolecule are automatically assigned via the graphical user interface (GUI) of the MedeA software environment (version 2.21). Then, the kerogen macromolecule structure is relaxed through the "Simple Force Field Minimization" and "Simple Force Field Dynamics" modules of MedeA. We placed 12 kerogen macromolecules



DOI: 10.1021/acs.jpcc.8b07123
J. Phys. Chem. C 2018, 122, 23528−23542

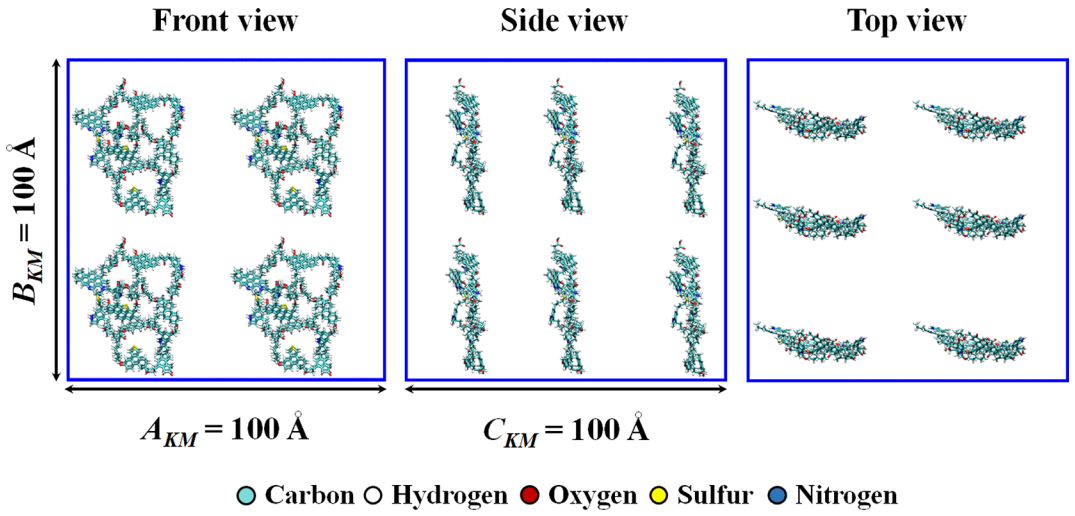


**Figure 3.** Initial orthorhombic simulation box: front, side, and top views of a cell with dimensions 100 × 100 × 100 Å$^3$.

inside an orthorhombic cell of dimensions 100 × 100 × 100 Å$^3$ (initial cell density is 0.08 g cm$^{-3}$). The initial positions of the kerogen macromolecules are shown in Figure 3.

In contrast to the work by Michalec and Lísal,[31] Sun et al.,[53] and Ungerer's MD relaxation procedure,[45,47] we did not start the first stage at high temperature. We added two first stages: (i) MD simulation in the NVT ensemble at $T$ = 300 K was performed on the initial orthorhombic simulation box during 100 ps to bring the system to the lowest energy state, and (ii) the temperature was increased during 100 ps in order to reach a target temperature $T_{\text{Target}}$ ($T_{\text{Target}}$ = 1000 K). Another simulation of 100 ps in the NVT ensemble was added to bring the system to equilibrium. This allows the system to surmount energetic barriers and explore the configurational space in order to find the configuration with the lowest energy. After that, the system was relaxed step by step in the isothermal−isobaric ensemble[77] at 100 atm through three decreasing temperature stages (700, 500, and 300 K), and each step duration was 100 ps, in the isotropic boxes. One step before the last, a MD simulation in the NPT ensemble at $T$ = 300 K was performed to reduce the pressure from 100 to 1 atm. At last, the temperature and the pressure were, respectively, kept at 300 K and 1 atm with a simulation time equal to 300 ps (150 ps equilibration + 150 ps production). During the 150 ps production, the kerogen matrix properties were calculated and averaged over 500 snapshots. The simulation time was long enough to ensure the relaxation of the configurational energy and the system density to reach equilibrium. The whole MD relaxation process to create the kerogen matrix is summarized in Table 1. In the construction of the system's configuration, dummy particles of varying size ($\sigma_{\text{DP}}$ = 5, 10, 15, 20, and 25 Å) were introduced to create different micro- and mesoporosity of the kerogen microstructures. From the initial configuration (Figure 3), 5 other boxes containing each one DP were generated. The DP was randomly placed in the simulation box. The same MD relaxation procedure was applied in all systems containing one DP. At the end of the MD relaxation procedure, the DP was removed from the compressed kerogen structure, leaving an empty space where gas adsorption is likely to occur. For the system using the largest dummy particle, another simulation of 1 ns in the NVT ensemble was added to relax the system. It was found that the difference between the accessible surface and the porosity found with and without this new relaxation step was similar (less than 1.6% difference). Therefore, we did not use this extra MD simulation. The final configuration of each kerogen matrix is depicted in Figure S1.

**Table 1. Molecular Dynamics Relaxation Procedure to Generate Kerogen Matrix Structures**

| stage | ensemble | temperature [K] | pressure [atm] | time [ps] |
|---|---|---|---|---|
| 1 | NVT | 300 | – | 100 |
| 2 | NVT | 300 → 1000 | – | 100 |
| 3 | NVT | 1000 | – | 100 |
| 4 | NPT | 1000 → 700 | 100 | 100 |
| 5 | NPT | 700 → 500 | 100 | 100 |
| 6 | NPT | 500 → 300 | 100 | 100 |
| 7 | NPT | 300 | 100 → 1 | 100 |
| 8 | NPT | 300 | 1 | 300 |

**Kerogen Slit Nanopore.** One configuration of the kerogen matrix without a dummy particle (Figure 4a) and one using the largest dummy particle ($\sigma_{\text{DP}}$ = 25 Å), with the average properties (density, porosity, and accessible surface), were selected to create our kerogen slit nanopores. The GUI of MedeA was used to extend the box in the $C_{\text{SPBox}}$-direction to $C_{\text{SPBox}}$ = 100 Å. A wall of 400 dummy particles ($\sigma_{\text{DPWall}}$ = 1 Å) was placed at one end of the simulation box (Figure 4b). Then, all the atoms were translated to bring the wall of dummy particles at the center of the simulation box (Figure 4c). The dummy particle wall is used to create, at the end of the MD relaxation procedure, an empty space between the two kerogen surfaces. The largest dummy particle ($\sigma_{\text{DP}}$ = 25 Å) was kept inside the simulation box in order to generate a kerogen slit nanopore with a rough surface. The initial kerogen slit nanopore boxes are presented in Figure S2. A simulation in the NVT ensemble at $T$ = 300 K was performed during 100 ps to bring the system to the lowest energy state. Then, the temperature was increased during 100 ps in order to reach a target temperature ($T_{\text{Target}}$ = 2000 K). From there, another 100 ps was added to bring the system to equilibrium. After that, 2 annealing cycles were realized between $T_{\text{Target}}$ and $T$ = 1000 K, in the $\text{NP}_{C_{\text{SPBox}}}T$ ensemble at 100 atm (the $A_{\text{SPBox}}$- and $B_{\text{SPBox}}$-direction are fixed, and the $C_{\text{SPBox}}$-direction can fluctuate). The systems were then relaxed by decreasing the temperature (400 ps). One step before the last, a simulation in the $\text{NP}_{C_{\text{SPBox}}}T$ ensemble at $T$ = 300 K was performed to reduce the pressure from 100 to 1 atm. Finally, the pressure and the



DOI: 10.1021/acs.jpcc.8b07123
J. Phys. Chem. C 2018, 122, 23528−23542

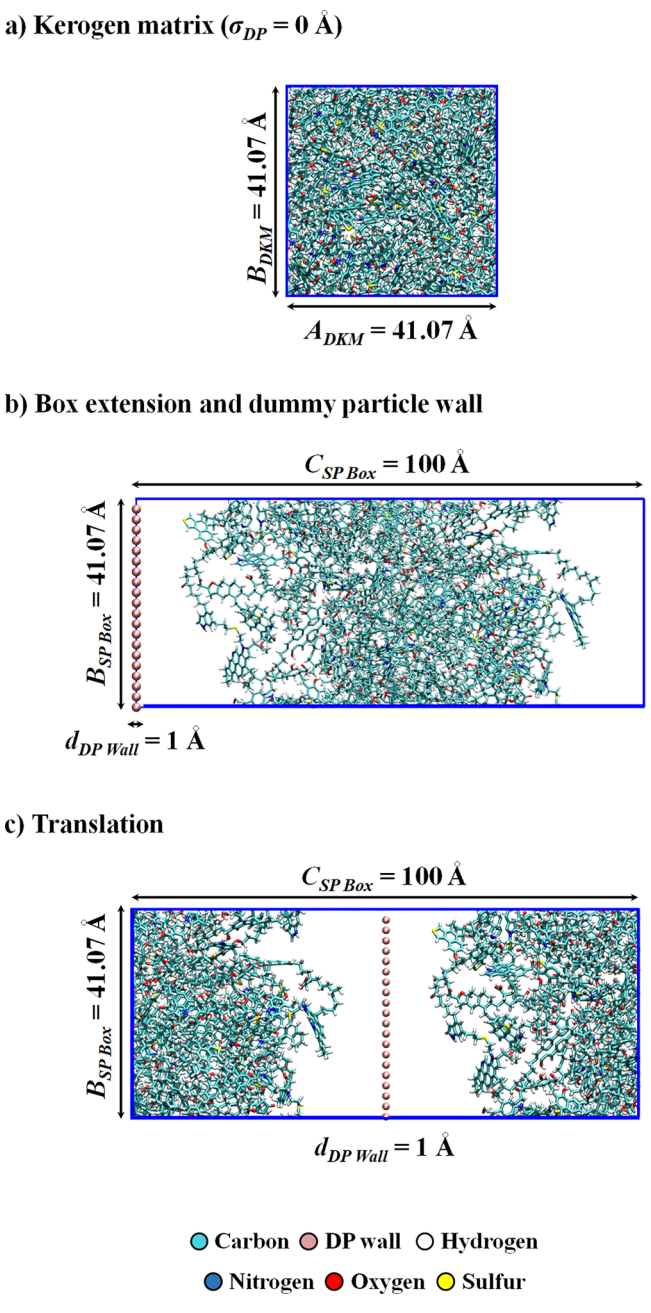


**Figure 4.** Steps to create a kerogen slit nanopore: (a) kerogen matrix ($\sigma_{DP}$ = 0 Å), (b) box extension and dummy particle wall, and (c) translation. $C_{SPBox}$ and $B_{SPBox}$ are the lattice parameters of the simulation box.

temperature were, respectively, kept at 1 atm and 300 K with a simulation time of 300 ps. During the 150 ps production, 500 snapshots were realized. The dummy particle wall was removed to have an empty space between the two kerogen surfaces. The space was changed to allow the desired distance. In this work, the width of our kerogen slit nanopores is set to 20 Å (this corresponds to the distance between the center of mass of the very last atoms from each surface). The configurations of the three slit nanopores used in our work are presented in Figure 5. The smooth slit nanopore will be presented shortly. The steps to create the kerogen slit nanopores are summarized in Table 2. The parameters of the MD simulations are the same in the kerogen matrix and in the slit nanopores. For the smooth slit nanopore the details are provided next.

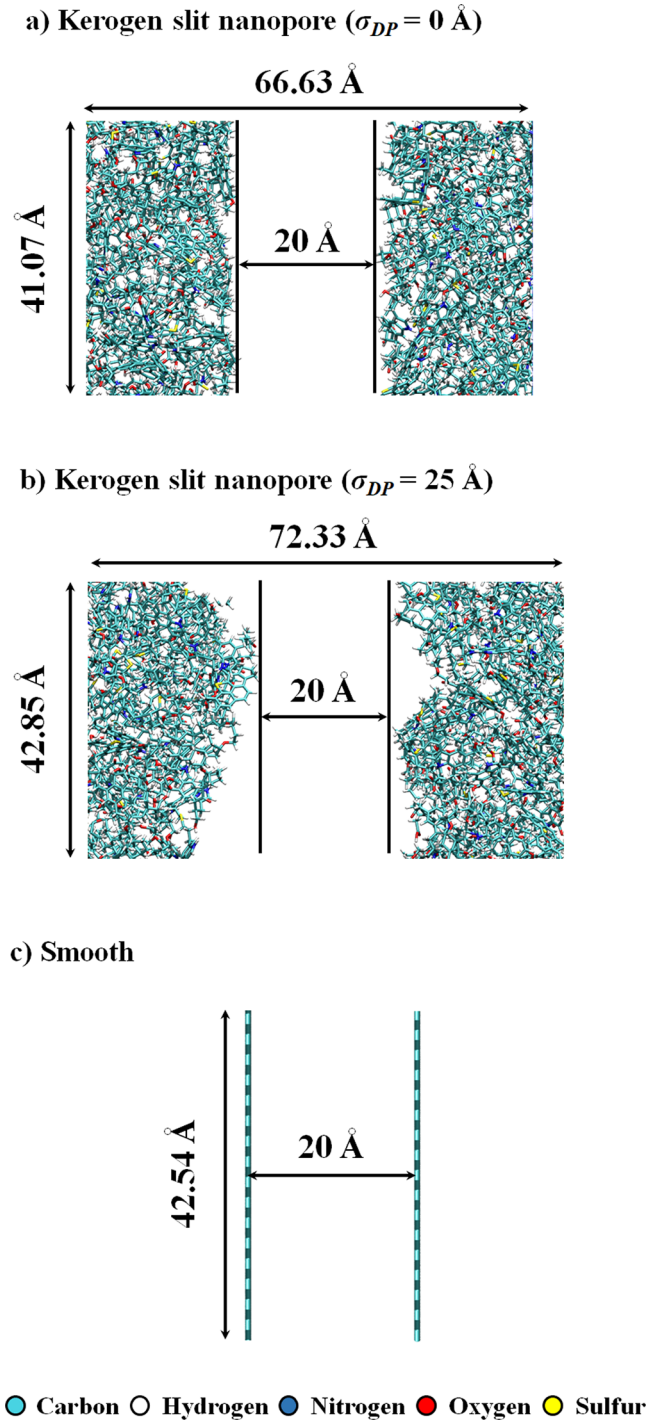


**Figure 5.** Three kerogen slit nanopores: (a) kerogen slit nanopore ($\sigma_{DP}$ = 0 Å), (b) kerogen slit nanopore ($\sigma_{DP}$ = 25 Å), and (c) smooth.

For a smooth surface, we used a graphite structure. The graphite is composed of carbon sheets stacked on top of each other to form layers. Our graphite is formed by two carbon sheets. The dimensions of the orthorhombic graphite simulation box are 41.75 × 42.54 × 23.348 Å$^3$, and the interlayer spacing is 20 Å (corresponding to the distance between the center of mass of each carbon sheet). The smooth nanopore, "Smooth", is presented in Figure 5c.

## RESULTS AND DISCUSSION

**Kerogen Matrix.** *Structure Characterization.* We analyzed the microstructure of our kerogen matrices at 300 K and 1 atm to



DOI: 10.1021/acs.jpcc.8b07123
J. Phys. Chem. C 2018, 122, 23528−23542

**Table 2. Molecular Dynamics Relaxation Procedure to Create Kerogen Slit Nanopores**

| stage | ensemble | temperature [K] | pressure [atm] | time [ps] |
|---|---|---|---|---|
| 1 | NVT | 300 | – | 100 |
| 2 | NVT | 300 → 2000 | – | 100 |
| 3 | NVT | 2000 | – | 100 |
| 4 | $NP_{C_{SPBox}}T$ | 2000 → 1000 | 100 | 100 |
| 5 | $NP_{C_{SPBox}}T$ | 1000 → 2000 | 100 | 100 |
| 6 | $NP_{C_{SPBox}}T$ | 2000 → 1000 | 100 | 100 |
| 7 | $NP_{C_{SPBox}}T$ | 1000 → 2000 | 100 | 100 |
| 8 | $NP_{C_{SPBox}}T$ | 2000 → 300 | 100 | 400 |
| 9 | $NP_{C_{SPBox}}T$ | 300 | 100 → 1 | 100 |
| 10 | $NP_{C_{SPBox}}T$ | 300 | 1 | 300 |

investigate the effects of the dummy particle. We also studied the microstructure of our kerogen matrices at 300 K and pressures to 150 atm to investigate the effect of pressure. The difference in the microstructure properties (porosity, accessible surface area, and the largest pore radius) in different simulations is included in the standard deviation (Table S2). The pressure seems only to affect the surface area not the largest pore radius. The lattice parameters ($A_{KM}$, $B_{KM}$, and $C_{KM}$) and density of the kerogen matrix ($\rho_{KM}$) are summarized in Table 3. The lattice parameters of the largest simulation box are presented in Figure 6a. The density decreases from 1.12 ± 0.01 g cm$^{-3}$ to 0.99 ± 0.04 g cm$^{-3}$ when increasing the dummy particle size. The larger the size of the dummy particle, the higher the empty space will be. This result is in agreement with simulated results from Sui et al.[13] (1.0 g cm$^{-3}$), Zhao et al.[39] (1.12 g cm$^{-3}$), Wang et al.[38] (1.073 g cm$^{-3}$), and Huang et al.[42] (1.07 g cm$^{-3}$), who used the same kerogen macromolecule (without controlling the porosity of their kerogen matrix).

The porosity and accessible surface area calculated from methane probe particles are reported in Table 3, and the methane-accessible surface area of each kerogen matrix is exposed in Figure S3. The results based on the nitrogen probe particle are close to the methane probe particle because the size of both probe particles is close. The porosity and accessible surface area calculated from nitrogen probe particles are listed in Table S3. The results show that the porosity and the methane-accessible surface area increase, respectively, from 0.02 ± 0.01% to 3.9 ± 0.2% ($\sigma_{DP}$ = 25 Å) and from 10 ± 3 m$^2$ g$^{-1}$ to 320 ± 12 m$^2$ g$^{-1}$ ($\sigma_{DP}$ = 25 Å) with increasing the dummy particle size. The same trend is observed by Collell et al.[47] (using $\sigma_{DP}$ = 0, 9, 11, 13, 15, and 17 Å), Michalec and Lísal[31] (using $\sigma_{DP}$ = 0, 9, 11, 13, and 15 Å), and Vasileiadis et al.[37] (using $\sigma_{DP}$ = 0, 15, 20, 30, and 40 Å). These authors used the same method as in our work to alter the kerogen porosity.

The largest pore sizes are reported in Table 3. The pore size distributions are plotted in Figure 7. The result shows that the largest pore size increases from 2.69 ± 0.01 Å to 7.96 ± 0.01 Å ($\sigma_{DP}$ = 25 Å) with increasing dummy particle size. This is in agreement with simulations by Collell et al.[45] (6.44 ± 0.01 Å using $\sigma_{DP}$ = 15 Å), Michalec and Lísal[31] (6.75 ± 0.01 Å using $\sigma_{DP}$ = 15 Å), and Vasileiadis et al.[37] (5.7–6.9 ± 0.8–2.2 Å using $\sigma_{DP}$ = 15 Å). The PSD reveals that $\sigma_{DP}$ = 0, 5, and 10 Å give ultramicropores, and $\sigma_{DP}$ = 15, 20, and 25 Å create ultramicropores and micropores. All of our created porous media have a

**Table 3. Structure Characterization**[a]

| dummy particle diameter [Å] | lattice parameters [Å] | density [g cm$^{-3}$] | porosity [%] | methane accessible surface area [m$^2$ g$^{-1}$] | largest pore radius [Å] |
|---|---|---|---|---|---|
| – | 41.07 ± 0.04 | 1.12 ± 0.01 | 0.02 ± 0.01 | 10 ± 3 | 2.69 ± 0.01 |
| 5 | 41.09 ± 0.05 | 1.12 ± 0.04 | 0.11 ± 0.02 | 36 ± 5 | 3.29 ± 0.01 |
| 10 | 41.43 ± 0.05 | 1.09 ± 0.04 | 0.67 ± 0.06 | 86 ± 4 | 4.55 ± 0.01 |
| 15 | 41.54 ± 0.05 | 1.08 ± 0.04 | 1.16 ± 0.07 | 101 ± 4 | 6.06 ± 0.01 |
| 20 | 41.83 ± 0.06 | 1.06 ± 0.04 | 2.23 ± 0.09 | 163 ± 5 | 7.24 ± 0.01 |
| 25 | 42.85 ± 0.07 | 0.99 ± 0.04 | 3.9 ± 0.2 | 320 ± 12 | 7.96 ± 0.01 |

[a]Porosity and accessible surface area are calculated from methane probe particles at $T$ = 300 K and $P$ = 1 atm.

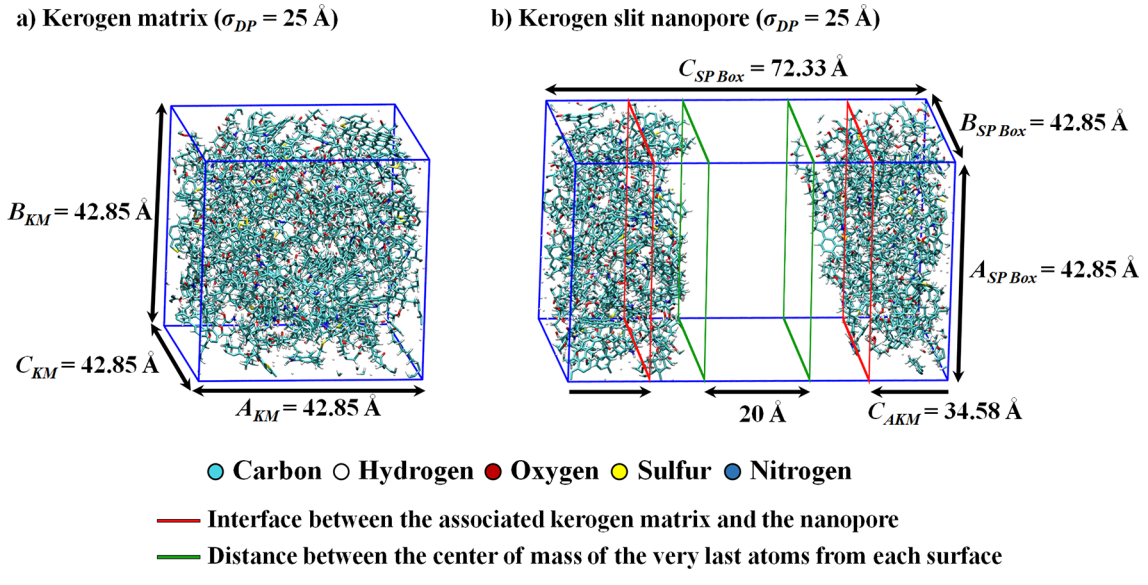


**Figure 6.** Lattice parameters of the (a) kerogen matrix and (b) kerogen slit nanopore.



DOI: 10.1021/acs.jpcc.8b07123
J. Phys. Chem. C 2018, 122, 23528–23542

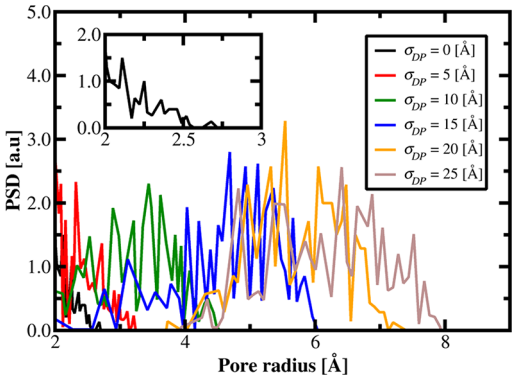


**Figure 7.** Pore size distribution of kerogen matrices created with different dummy particles.

poor network. Despite this, methane can diffuse through the matrix when the kerogen molecules are flexible as we will show later.

*Methane Adsorption in a Rigid and Flexible Kerogen Matrix.* We analyzed the methane adsorption isotherms in the rigid kerogen matrix at three different temperatures ($T$ = 333.15, 363.15, and 393.15 K) and pressures to 140 atm to investigate the effects of temperature. The $CH_4$ adsorption isotherm is also investigated in a rigid and flexible kerogen matrix at 333.15 K and pressure up to 400 atm to examine the effect of kerogen molecular flexibility. The system with the largest accessible surface area was selected. Absolute adsorption, representing the number of methane molecules in the adsorbed phase in the rigid kerogen matrix, is plotted in Figure 8a. The excess adsorptions and Langmuir fitting curves are, respectively, plotted in Figures S4 and S5. Figure 8a shows that the absolute adsorption at 140 atm is $2.47 \times 10^{-3}$ mmol m$^{-2}$ at 333.15 K, $2.00 \times 10^{-3}$ mmol m$^{-2}$ at 363.15 K, and $1.55 \times 10^{-3}$ mmol m$^{-2}$ at 393.15 K. These results are in agreement with the general observation that absolute adsorption increases with increasing pressure but decreases with increasing temperature. The trends are consistent with experiments[25,27,78] and molecular simulations.[13,39,42]

Figure 8b shows that when the pressure is ~200 atm, at 333.15 K, the absolute adsorption in the rigid kerogen matrix reaches a plateau of $2.57 \times 10^{-3}$ mmol m$^{-2}$, whereas the methane absolute adsorption in the flexible kerogen matrix increases to ~350 atm; it reaches a plateau of $4.03 \times 10^{-3}$ mmol m$^{-2}$. Absolute adsorption of $CH_4$ in the flexible kerogen is ~1.57 times higher than in the rigid kerogen. At 1 atm, rigid and flexible kerogen structures have, respectively, methane-accessible surface areas of 320 m$^2$ g$^{-1}$ and 317 m$^2$ g$^{-1}$. Upon gas adsorption, in the flexible kerogen structure, the methane-accessible surface area increases to 342 m$^2$ g$^{-1}$ at 200 atm (Figure 9a). With increasing pressure, kerogen microstructure changes, and the accessible space increases. Note the sudden change in the slope of the accessible surface area of around 120 atm. This could be due to a change in structure. This observation is supported by the pore size distribution (Figure 9b). The kerogen molecular flexibility has a significant effect on adsorption. These results have the same trend as found by Ho et al.[41] in the type II-D kerogen matrix.

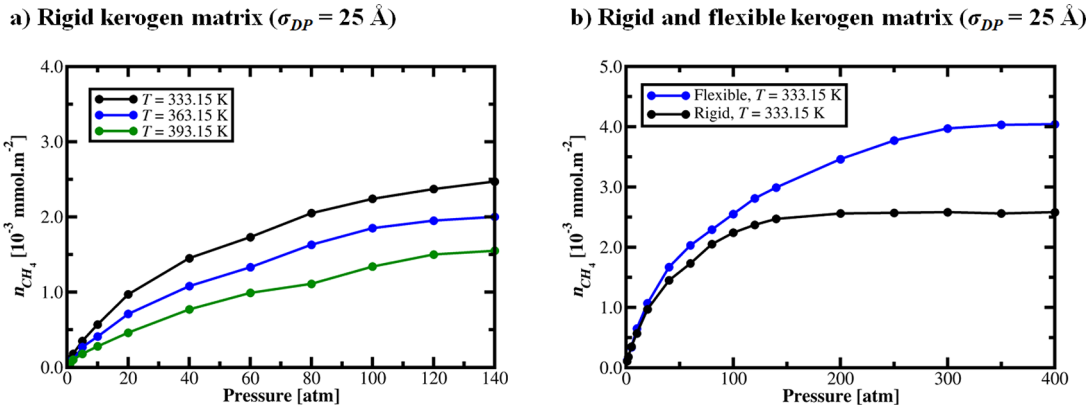


**Figure 8.** Methane absolute adsorption in the kerogen matrix at different temperatures: (a) rigid kerogen matrix and (b) flexible and rigid kerogen matrix.

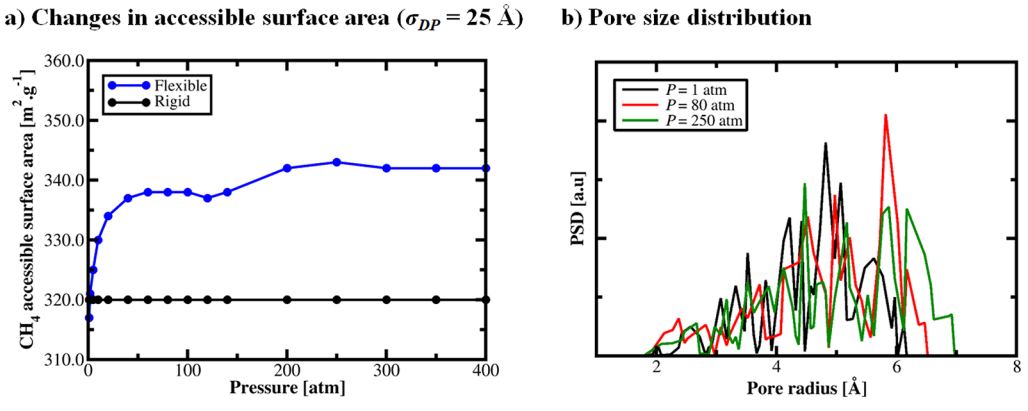


**Figure 9.** Changes in the kerogen matrix: (a) methane-accessible surface area versus pressure and (b) pore size distribution at different pressures and $T$ = 333.15 K.



DOI: 10.1021/acs.jpcc.8b07123
J. Phys. Chem. C 2018, 122, 23528−23542

**Table 4. Rugosity Parameters of Surfaces of the Slit Nanopores**

| surface roughness | surface | amplitude [Å] | maximum depth [Å] | maximum height [Å] |
|---|---|---|---|---|
| smooth | top | 0.3 | 0.2 | 0.1 |
| | bottom | 0.3 | 0.2 | 0.1 |
| moderately rough | top | 13.8 | 10.7 | 3.1 |
| | bottom | 10.1 | 7.5 | 2.6 |
| rough | top | 21.9 | 14.0 | 7.9 |
| | bottom | 18.1 | 13.2 | 4.9 |

Vasileiadis et al.[44] indicated that methane adsorption in the rigid and flexible kerogen matrix is very close (1.91 mmol $g^{-1}$ and 1.93 mmol $g^{-1}$, respectively) in type II-D kerogen macromolecules. Their conclusion is based on the results at a pressure of 20 atm at 298.15 K. As observed in Figure 8b, methane adsorption in the rigid and flexible kerogen matrix is somewhat close ($0.97 \times 10^{-3}$ mmol $m^{-2}$ and $1.07 \times 10^{-3}$ mmol $m^{-2}$, respectively) at 20 atm. The absolute adsorption difference in the rigid and flexible kerogen matrix increases with increasing pressure. The difference between Vasileiadis et al.[44] and our results at 20 atm may be because of a different type of kerogen macromolecule in our simulations.

**Slit Nanopores.** *Structure Characterization.* We analyzed the rugosity of the rigid slit nanopores to study methane adsorption. The rugosity parameters, i.e., the amplitude (maximum height of the roughness profile), the maximum depth, and the maximum height from methane probe particles, are presented in Table 4. Figure 10 presents the slit nanopore surfaces. The amplitude, the maximum depth, and the maximum height increase from 0.3 Å to 21.9 Å, 0.2 Å to 14.0 Å, and 0.1 Å to 7.9 Å, respectively, with increasing surface roughness. The surface roughness of the kerogen slit nanopores without dummy particle (Figure 5a) and with the largest dummy particle (Figure 5b) are, respectively, referred as to "moderately rough" (Figure 10b) and "rough" (Figure 10c).

We also analyzed the microstructure of our slit kerogen nanopores and associated kerogen matrix at 300 K and 1 atm to

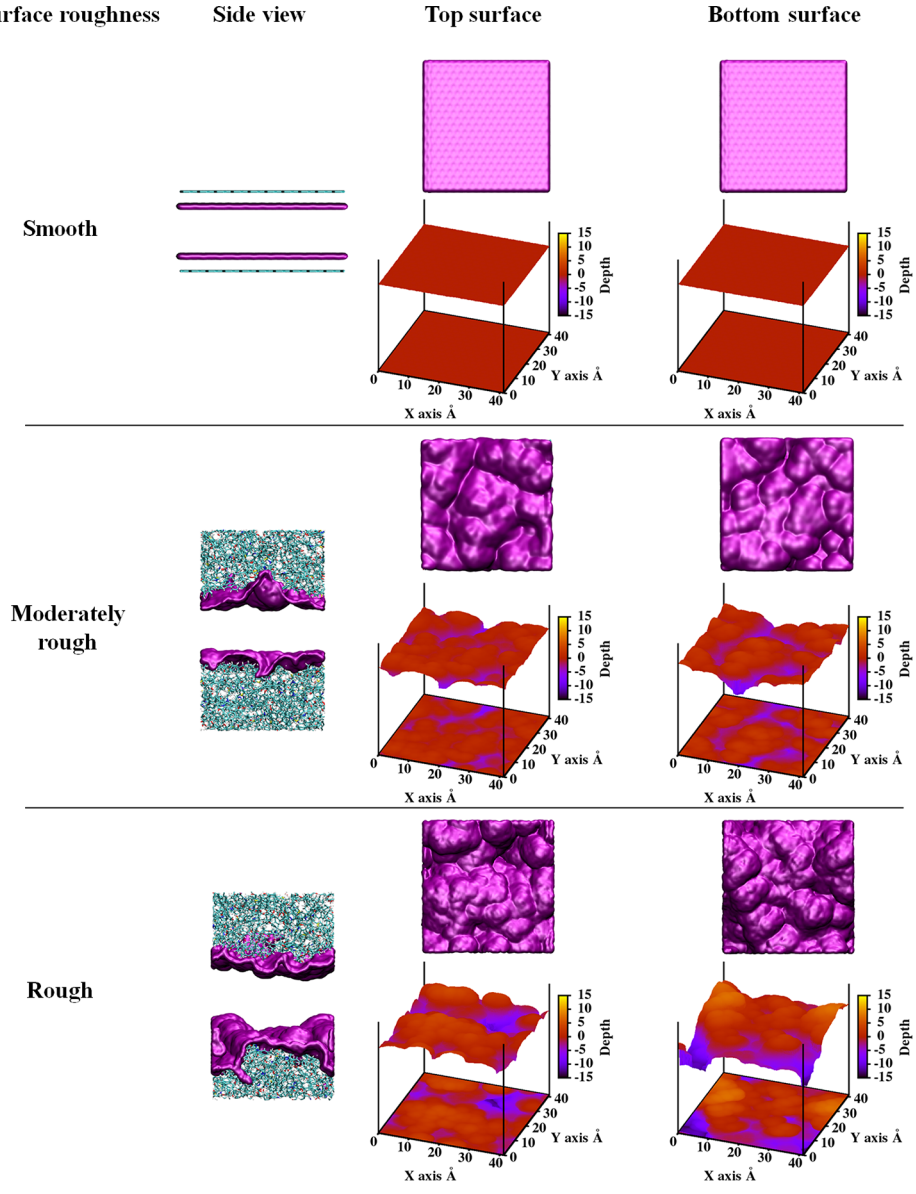


**Figure 10.** Side, top, and bottom views of the surface (in purple) and 3D and 2D roughness profiles of each slit nanopore: (a) smooth, (b) moderately rough, and (c) rough.



DOI: 10.1021/acs.jpcc.8b07123
J. Phys. Chem. C 2018, 122, 23528−23542

**Table 5. Lattice Parameters of the Slit Nanopores and the Associated Kerogen Matrix**

| | simulation box lattice parameters | | | associated kerogen matrix lattice parameter | associated kerogen matrix density |
|---|---|---|---|---|---|
| surface roughness | $A_{SPBox}$ [Å] | $B_{SPBox}$ [Å] | $C_{SPBox}$ [Å] | $C_{AKM}$ [Å] | $\rho_{AKM}$ [g cm$^{-3}$] |
| smooth | 41.75 | 42.54 | 23.348 | – | – |
| moderately rough | 41.07 | 41.07 | 66.63 ± 0.04 | 42.17 ± 0.04 | 1.07 ± 0.02 |
| rough | 42.85 | 42.85 | 72.33 ± 0.04 | 34.58 ± 0.04 | 0.97 ± 0.02 |

determine the interface between the associated kerogen matrix and the slit space. The lattice parameters of the box of the slit pores ($A_{SPBox}$, $B_{SPBox}$, $C_{SPBox}$) are provided in Table 5. Figures 11a and 11b show, respectively, the density profile of the associated kerogen matrix and the moderately rough and rough slit pores. We like to point out that slit nanopores are not connected to a kerogen rock matrix. However, in order to study both in the same simulations we connect them. As stated earlier, slit pores are a physical model for the more complex nanoporous matrix. The density profiles are divided in two equal parts by a purple dashed line. In the left side, the average density of the associated kerogen matrix is calculated and plotted from $C_{SPBox}$ = 0 Å to the purple dashed line. In the right side, the average density of the associated kerogen matrix is calculated and plotted from the very end of the simulation box to the purple dashed line. When the slope of density plots shows a pronounced change, the interface between the slit pore and the associated kerogen matrix is defined. The lattice parameter ($C_{AKM}$) and the density ($\rho_{AKM}$) of the associated kerogen matrix are listed in Table 5. The lattice parameters of the rough kerogen slit nanopore are presented in Figure 6b. Table 5 shows that the density of the associated kerogen matrix is, respectively, 1.07 ± 0.02 g cm$^{-3}$ and 0.97 ± 0.02 g cm$^{-3}$ for the moderately rough and rough systems. In the latter we used a dummy particle to generate it. Note that these densities are in line with the results in Table 3.

*Methane Adsorption in Rigid and Flexible Slit Nanopores.* We analyzed the methane adsorption isotherms in rigid slit nanopores. The $CH_4$ adsorption isotherm is also investigated in rigid slit nanopores at 333.15 K to a pressure of 300 atm to examine the effects of the chemical and roughness of the surface. At 333.15 K and 300 atm, we investigated the effects of the kerogen molecular flexibility in a moderately rough slit nanopore. The density profiles of methane in different slit nanopores at 333.15 K are plotted in Figure 12, as well as snapshots corresponding to one configuration at 300 atm. The results at 363.15 and 393.15 K are plotted in Figures S6, S7, and S8. Figure 12a shows well-structured methane adsorption layers on each surface. These results are in agreement with other density profiles using the same type of slit nanopore,[50,52] as well as the same trend as in clays.[79−81] $CH_4$ forms a weak second adsorption layer at pressures above 40 atm. Figures 12b and 12c show methane adsorption layers on the kerogen slit nanopore surfaces. These results have the same trend as by Sun et al.[53] who used a kerogen slit nanopore based on mature kerogen fragments.[45] There is no second adsorption layer, and a higher number of methane molecules are in the middle of the nonsmooth slit nanopores than in the smooth slit nanopore. This may be explained by the physicochemical properties of the nanopore surfaces. The interactions between the adsorbent and the adsorbate consist of the dispersion−repulsion interactions (represented by the 9-6 LJ potential) and the Coulombic interactions. The smooth slit nanopore surfaces are composed exclusively of carbon atoms ($q_{Carbon\ graphite}$ = 0 e). Thus, methane molecules can be readily adsorbed anywhere on the smooth slit nanopore surfaces. The moderately rough and rough slit nanopore surfaces are mostly composed of hydrogen atoms, partially composed of carbon

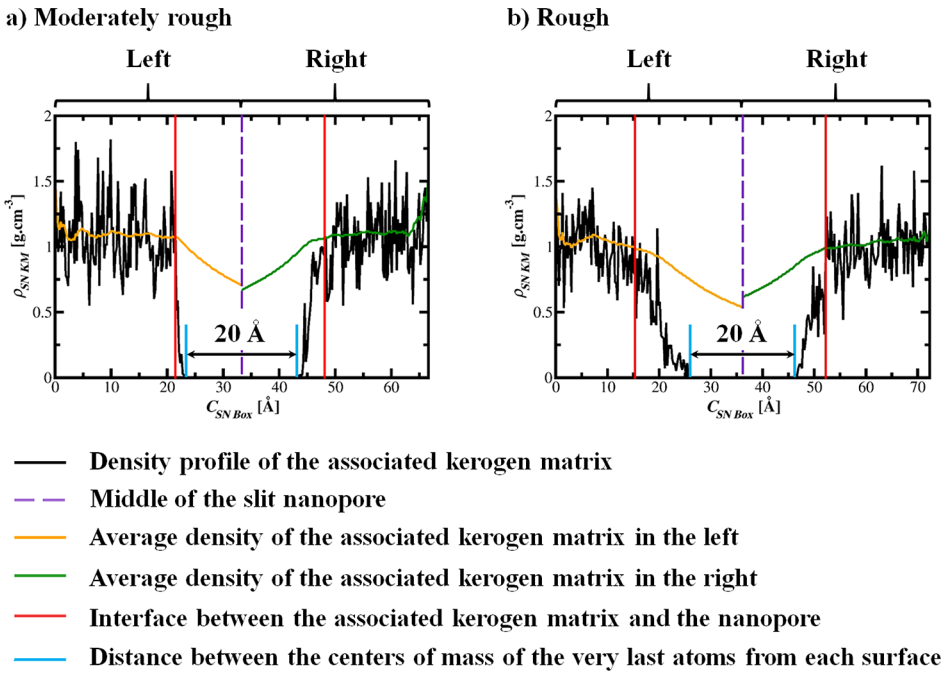


**Figure 11.** Density profile of the associated kerogen matrix: (a) moderately rough and (b) rough.



DOI: 10.1021/acs.jpcc.8b07123
J. Phys. Chem. C 2018, 122, 23528−23542

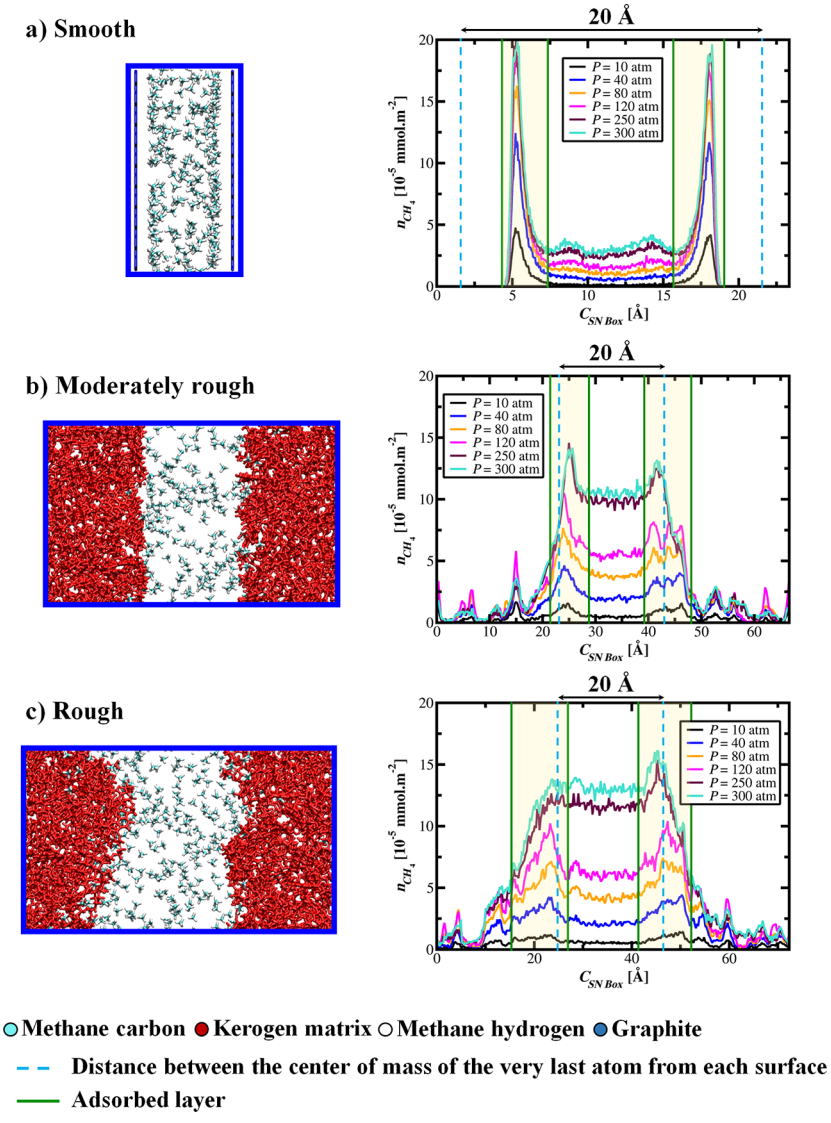


**Figure 12.** Density profile of methane in rigid slit nanopores at various pressures and at $T$ = 333.15 K. (a) Smooth slit nanopore. (b) Moderately rough slit nanopore. (c) Rough slit nanopore. The snapshots correspond to configuration on the left at $P$ = 300 atm.

atoms, and a few oxygen, sulfur, and nitrogen atoms. Thus, methane molecules tend to be pushed from the surfaces and end up in the middle of the pore. The $CH_4$ adsorption is impacted by the surface chemistry. These results have the same trend as found by Psarras et al.[82] in four different graphitic surfaces (pure graphitic surface, hydrated monovacancy, hydroxyl group, and a carboxyl group), by Billemont et al.[83] in two different carbon nanoporous media CS1000A and CS1000AF and by Huang et al.[42] in different kerogen types (chemical structure varies). Figures 12b and 12c shed light on the importance of roughness on surface adsorption. The rougher the surface and the higher the pressure, the lesser the adsorbed and free molecules can be distinguished. Figures 12a and 12b help to distinguish three different regions: the solid region (graphite or associated kerogen matrix), the interface region (methane adsorbed layer), and the central region (methane free molecules).

The absolute adsorptions, representing the number of methane molecules in the interface region from the slit nanopores, are plotted in Figures 13a and 13b. Because of the surface roughness of the rough slit nanopore (Figure 12c) the methane adsorption layer can not be well-defined, and it becomes difficult to distinguish the adsorbed molecules from the free molecules at pressures higher than 250 atm. For the rough slit nanopore, the adsorption is plotted in Figure 13c. Snapshots corresponding to the surface in the $A_{SPBox}$- and $B_{SPBox}$-direction of one configuration at 300 atm are presented in Figures 13a, 13b, and 13c. The methane absolute adsorption is higher on the smooth slit nanopore surfaces than on the moderately rough slit nanopore surfaces. This may be explained by the surface properties and surface roughness differences between the slit nanopore models, as analyzed above. The absolute adsorptions normalized by the accessible volume of the interface region are plotted in Figure S9. Figure 14 shows that absolute adsorption on a smooth and moderately rough rigid slit nanopore reaches a plateau at 5.02 × $10^{-3}$ mmol $m^{-2}$ and 3.53 × $10^{-3}$ mmol $m^{-2}$ at 250 atm and 333.15 K, respectively. The smooth slit nanopore surfaces adsorb ∼1.42 times more methane molecules than the moderately rough rigid slit nanopore. At 300 atm, the kerogen flexibility slightly affects methane adsorption at the rigid (3.58 × $10^{-3}$ mmol $m^{-2}$) and the flexible (3.75 × $10^{-3}$ mmol $m^{-2}$) moderately rough slit nanopore. Figure 14 also shows that methane adsorption at the moderately rough slit nanopore rigid


DOI: 10.1021/acs.jpcc.8b07123
J. Phys. Chem. C 2018, 122, 23528−23542

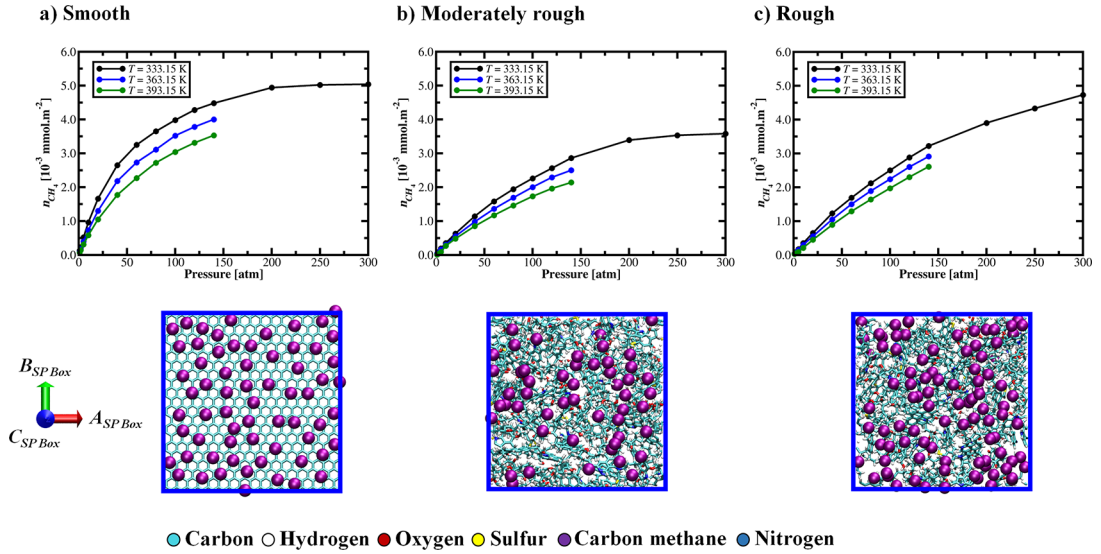


**Figure 13.** Methane absolute adsorption in the: (a) rigid smooth slit nanopore, (b) moderately rough rigid slit nanopore, and (c) rough rigid slit nanopore at different temperatures. In the rough slit nanopore, adsorbed and free molecules can not be distinguished at high pressure. The snapshots correspond to the surfaces in the $A_{SPBox}$- and $B_{SPBox}$-direction at $P$ = 300 atm from rigid systems.

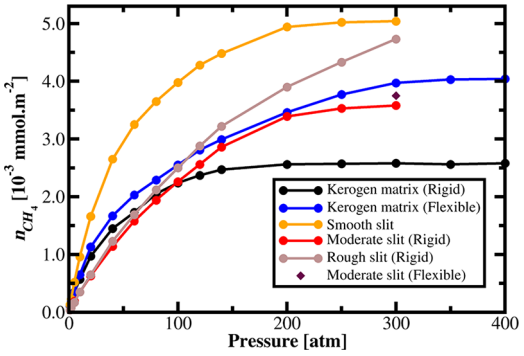


**Figure 14.** Methane adsorption versus pressure in slit nanopores and kerogen matrices at $T$ = 333.15 K. Note that smooth nanopores are assumed rigid in the figure and throughout in this work.

and flexible states is close to methane adsorption in the flexible kerogen matrix ($3.97 \times 10^{-3}$ mmol m$^{-2}$) at 300 atm, whereas absolute methane adsorption in the smooth slit nanopore is higher than the absolute adsorption in the rigid and flexible kerogen matrix. The physicochemical properties and surface roughness are important considerations in relating adsorption in the slit nanopore and kerogen matrix.

**Methane Self-Diffusion.** We analyzed methane mobility and self-diffusion in the flexible kerogen matrix and flexible slit nanopores at $T$ = 333.15 K and $P$ = 140 atm. To this end, one configuration of each flexible system at equilibrium was selected from the MD-GCMC simulations. Then, MD simulations in the NVT ensemble were performed during 10 ns. The microscopic methane self-diffusion was investigated by eq 5 and eq 6. The MSD was calculated for the last 5 ns of the trajectory. For the slit nanopores, the MSD of methane molecules is calculated in each region. The methane self-diffusion coefficients in each system are presented in Table 6. The table shows that the mobility of $CH_4$ decreases by 2 orders of magnitude from the central slit to the matrix ($D_{Central} \geq D_{Interface} \geq D_{Associated\ kerogen\ matrix}$). The general trend is in agreement with the simulations by Sun et al.[53] The trend can be explained by the fact that in the solid region the methane molecules are confined in the pores of the kerogen

**Table 6. Methane Self-Diffusion Coefficient in the Central and Interface Regions of the Slit and the Associated Matrix (The Width of the Slit Nanopores is 20 Å)**

| | $CH_4$ self-diffusion coefficient | | |
|---|---|---|---|
| surface roughness | $D_{Central}$ [$\times 10^{-7}$ m$^2$ s$^{-1}$] | $D_{Interface}$ [$\times 10^{-7}$ m$^2$ s$^{-1}$] | $D_{Associated\ kerogen\ matrix}$ [$\times 10^{-9}$ m$^2$ s$^{-1}$] |
| smooth | 5.1 | 3.2 | – |
| moderately rough | 5.4 | 2.6 | 6.1 |
| rough | 5.2 | 2.2 | 7.1 |

matrix; in the interface region $CH_4$ molecules are adsorbed; and in the central slit pore region the methane molecules interact with each other. The surface roughness affects the self-diffusion coefficient in the interface region: the higher the surface roughness, the lower the mobility (Table 6). In our simulations the methane self-diffusion coefficient in the flexible kerogen matrix ($6.8 \times 10^{-9}$ m$^2$ s$^{-1}$) is close to the associated kerogen matrix from the moderately rough ($6.1 \times 10^{-9}$ m$^2$ s$^{-1}$) and rough ($7.1 \times 10^{-9}$ m$^2$ s$^{-1}$) systems. The order of magnitude of the methane self-diffusion coefficients in the matrix is in agreement with Collell et al.[47] ($4.8 \times 10^{-9}$ m$^2$ s$^{-1}$ at $T$ = 300 K and $P$ = 20 MPa) and Sui et al.[13] ($2.1 \times 10^{-9}$ m$^2$ s$^{-1}$ at $T$ = 340 K and $P$ = 15 MPa).

To further investigate methane diffusion through the kerogen slit nanopores and its associated kerogen matrix, methane molecules were followed throughout the MD simulations (Figure S10). The tracked methane molecule starts from an isolated pore, and the kerogen matrix deforms and creates paths, allowing the tracked methane molecule to go back and forth between the solid region and the central region.

## CONCLUSIONS

In this work we have proposed a new method to create kerogen slit nanopores based on the full kerogen macromolecules to investigate the effect of surface roughness and atomic structure on adsorption and self-diffusion. We used type II-A kerogen macromolecules in our creation. The method can be used with other types of kerogen molecules. By using a dummy particle we created a rough surface. Without the use of a dummy particle the


DOI: 10.1021/acs.jpcc.8b07123
J. Phys. Chem. C 2018, 122, 23528−23542

surface is moderately rough. We investigated adsorption and self-diffusion in three types of slit nanopores. One of the three is the conventional slit nanopore often used in the literature which is comprised of smooth carbon surfaces.

In addition to slit nanopores we also investigate adsorption and self-diffusion in the kerogen matrix of constant total volume. The constant total volume is an approximation for the kerogen matrix in the subsurface. We allow for flexibility of atoms in the kerogen matrix and carry computations to pressures higher than the values in the literature. Most computations are performed at three different temperatures. The maximum pressure in our work is 400 atm. Methane molecules are used in all of our calculations. The main findings from our work are:

1. The plateau of the methane absolute adsorption at 333.15 K in the rigid kerogen matrix is reached at ∼200 atm and ∼350 atm in the flexible kerogen matrix. The adsorption is about 57% higher in the flexible kerogen matrix than in the rigid matrix. The kerogen matrix is a dynamic system, and a coupling may exist between gas adsorption and kerogen matrix structure deformation.
2. Adsorption in the kerogen matrix and in the slit nanopore (per unit surface area) may not be the same. In the smooth nanopore, a clear adsorption layer develops. A second weak adsorption layer may also develop at high pressure. In the kerogen slit nanopores, sharp adsorption layers are not developed. In the rough and moderately rough slit nanopores, the density of methane in the middle of the slit is higher than the density at the center of the smooth nanopore. In the rough slit nanopore, the adsorption layer is not well-defined, and adsorbed and free molecules can not be distinguished at high pressure. The absolute adsorption is about 42% higher in the smooth slit nanopore than the moderately rough slit nanopore. These results are for a 2 nm wide slit pore.
3. The methane self-diffusion coefficient decreases 2 orders of magnitude from the center of the slit pore to the surface and the kerogen matrix. Our results indicate that the methane self-diffusion coefficient at the surfaces of slit nanopores is weakly affected by confinement and surface roughness.

## ■ ASSOCIATED CONTENT

### Supporting Information

The Supporting Information is available free of charge on the ACS Publications website at DOI: 10.1021/acs.jpcc.8b07123.

Type II-A kerogen model properties, pressure effects, porosity, and accessible surface area are calculated from nitrogen probe particles, final configurations of each kerogen matrix using $\sigma_{DP}$ = 5, 10, 15, 20, and 25 Å, initial and final configurations of each slit kerogen nanopore, methane-accessible surface area of each kerogen matrix, methane excess adsorption, Langmuir model, density profile of methane in smooth slit nanopore, density profile of methane in moderately rough slit nanopore, density profile of methane in rough slit nanopore, methane absolute adsorption normalized by the accessible volume of the adsorption layer, and tracked methane molecule in the moderately rough and rough slit nanopores (PDF)

## ■ AUTHOR INFORMATION


### Corresponding Author

*E-mail: abbas.firoozabadi@yale.edu. Phone: +1 (650) 326-9172.

### ORCID

Stéphane Tesson: 0000-0001-9045-1443

Abbas Firoozabadi: 0000-0001-6102-9534


### Notes

The authors declare no competing financial interest.

## ■ ACKNOWLEDGMENTS

Reservoir Engineering Research Institute greatly acknowledges financial support by Saudi Aramco (Project code: RGC/3/2053-01-01) at the King Abdullah Science and Technology University (KAUST). We also thank Dr. Ali Dogru of Aramco for technical discussions.

## ■ REFERENCES


(1) Boyer, C.; Clark, B.; Jochen, V.; Lewis, R.; Miller, C. K. Shale gas: A global resource. *Oilfield Rev.* **2011**, *23*, 28−39.

(2) Paylor, A. The social-economic impact of shale gas extraction: A global perspective. *Third World Quarterly* **2017**, *38*, 340−355.

(3) Stevens, P. The shale gas revolution: Developments and changes. *Energy Environ. Res.* **2012**.

(4) Interfax Energy. http://interfaxenergy.com (accessed March 22, 2018).

(5) Oil Price. https://oilprice.com (accessed March 12, 2018).

(6) Ren, J.; Tan, S.; Goodsite, M. E.; Sovacool, B. K.; Dong, L. Sustainability, shale gas, and energy transition in china: Assessing barriers and prioritizing strategic measures. *Energy* **2015**, *84*, 551−562.

(7) Howarth, R. W.; Ingraffea, A.; Engelder, T. Natural gas: Should fracking stop? *Nature* **2011**, *477*, 271−275.

(8) Yethiraj, A.; Striolo, A. Fracking: What can physical chemistry offer? *J. Phys. Chem. Lett.* **2013**, *4*, 687−690.

(9) Clarkson, C. R.; Solano, N.; Bustin, R. M.; Bustin, A. M. M.; Chalmers, G. R. L.; He, L.; Melnichenko, Y. B.; Radliński, A. P.; Blach, T. P. Pore structure characterization of north American shale gas reservoirs using USANS/SANS, gas adsorption, and mercury intrusion. *Fuel* **2013**, *103*, 606−616.

(10) Cao, T.; Song, Z.; Wang, S.; Cao, X.; Li, Y.; Xia, J. Characterizing the pore structure in the silurian and permian shales of the sichuan basin, china. *Mar. Pet. Geol.* **2015**, *61*, 140−150.

(11) Ungerer, P.; Collell, J.; Yiannourakou, M. Molecular modeling of the volumetric and thermodynamic properties of kerogen: Influence of organic type and maturity. *Energy Fuels* **2015**, *29*, 91−105.

(12) Durand, B. *Kerogen: Insoluble organic matter from sedimentary rocks*; Editions Technip, 1980.

(13) Sui, H.; Yao, J. Effect of surface chemistry for $CH_4/CO_2$ adsorption in kerogen: A molecular simulation study. *J. Nat. Gas Sci. Eng.* **2016**, *31*, 738−746.

(14) Orr, W. L. Kerogen/asphaltene/sulfur relationships in sulfur-rich monterey oils. *Org. Geochem.* **1986**, *10*, 499−516.

(15) Tissot, B. P.; Welte, D. H. In *Petroleum formation and occurrence*; Tokyo, B. H. N. Y., Ed.; Springer-Verlag, 1984; Vol. Second revised.

(16) Ganz, H.; Kalkreuth, W. Application of infrared spectroscopy to the classification of kerogentypes and the evaluation of source rock and oil shale potentials. *Fuel* **1987**, *66*, 708−711.

(17) Boyer, C.; Kieschnick, J.; Suarez-Rivera, R.; Lewis, R. E.; Waters, G. Producing gas from its source. *Oilfield Rev.* **2006**, *18*, 36−49.

(18) Bousige, C.; Ghimbeu, C. M.; Vix-Guterl, C.; Pomerantz, A. E.; Suleimenova, A.; Vaughan, G.; Garbarino, G.; Feygenson, M.; Wildgruber, C.; Ulm, F.-J.; et al. Realistic molecular model of kerogen's nanostructure. *Nat. Mater.* **2016**, *15*, 576−582.

(19) Etminan, S. R.; Javadpour, F.; Maini, B. B.; Chen, Z. Measurement of gas storage processes in shale and of the molecular diffusion coefficient in kerogen. *Int. J. Coal Geol.* **2014**, *123*, 10−19.

(20) Okiongbo, K. S.; Aplin, A. C.; Larter, S. R. Changes in type II kerogen density as a function of maturity: Evidence from the kimmeridge clay formation. *Energy Fuels* **2005**, *19*, 2495−2499.

(21) Tong, J.; Han, X.; Wang, S.; Jiang, X. Evaluation of structural characteristics of huadian oil shale kerogen using direct techniques




DOI: 10.1021/acs.jpcc.8b07123
J. Phys. Chem. C 2018, 122, 23528−23542

(solid-state 13C NMR, XPS, FT-IR, and XRD). *Energy Fuels* **2011**, *25*, 4006−4013.
(22) Gasparik, M.; Ghanizadeh, A.; Bertier, P.; Gensterblum, Y.; Bouw, S.; Krooss, B. M. High-pressure methane sorption isotherms of black shales from the netherlands. *Energy Fuels* **2012**, *26*, 4995−5004.
(23) Yan, J.; Jiang, X.; Han, X.; Liu, J. A TG-FTIR investigation to the catalytic effect of mineral matrix in oil shale on the pyrolysis and combustion of kerogen. *Fuel* **2013**, *104*, 307−317.
(24) Charoensuppanimit, P.; Mohammad, S. A.; Gasem, K. A. M. Measurements and modeling of gas adsorption on shales. *Energy Fuels* **2016**, *30*, 2309−2319.
(25) Tian, H.; Li, T.; Zhang, T.; Xiao, X. Characterization of methane adsorption on overmature lower silurian-upper ordovician shales in sichuan basin, southwest china: Experimental results and geological implications. *Int. J. Coal Geol.* **2016**, *156*, 36−49.
(26) Ji, W.; Song, Y.; Rui, Z.; Meng, M.; Huang, H. Pore characterization of isolated organic matter from high matured gas shale reservoir. *Int. J. Coal Geol.* **2017**, *174*, 31−40.
(27) Rexer, T. F.; Mathia, E. J.; Aplin, A. C.; Thomas, K. M. High-pressure methane adsorption and characterization of pores in posidonia shales and isolated kerogens. *Energy Fuels* **2014**, *28*, 2886−2901.
(28) Zhao, H.; Wu, T.; Firoozabadi, A. High pressure sorption of various hydrocarbons and carbon dioxide in kimmeridge blackstone and isolated kerogen. *Fuel* **2018**, *224*, 412−423.
(29) Wu, T.; Zhao, H.; Tesson, S.; Firoozabadi, A. Absolute adsorption of light hydrocarbons and carbon dioxide in shale rock and and isolated kerogen. *Fuel* **2019**, *235*, 855−867.
(30) Falk, K.; Pellenq, R.; Ulm, F. J.; Coasne, B. Effect of chain length and pore accessibility on alkane adsorption in kerogen. *Energy Fuels* **2015**, *29*, 7889−7896.
(31) Michalec, L.; Lísal, M. Molecular simulation of shale gas adsorption onto overmature type II model kerogen with control microporosity. *Mol. Phys.* **2017**, *115*, 1086−1103.
(32) Obliger, A.; Pellenq, R.; Ulm, F.-J.; Coasne, B. Free volume theory of hydrocarbon mixture transport in nanoporous materials. *J. Phys. Chem. Lett.* **2016**, *7*, 3712−3717.
(33) Ho, T. A.; Criscenti, L. J.; Wang, Y. Nanostructural control of methane release in kerogen and its implications to wellbore production decline. *Sci. Rep.* **2016**, *6*, 28053.
(34) Feng, F.; Akkutlu, I. Y. Molecular modeling of organic materials for flow simulation and digital source-rock physics. *SPE Annual Technical Conference and Exhibition*; 2017.
(35) Pathak, M.; Kweon, H.; Deo, M.; Huang, H. Kerogen swelling and confinement: Its implication on fluid thermodynamic properties in shales. *Sci. Rep.* **2017**, *7*, 12530.
(36) Pathak, M.; Huang, H.; Meakin, P.; Deo, M. Molecular investigation of the interactions of carbon dioxide and methane with kerogen: Application in enhanced shale gas recovery. *J. Nat. Gas Sci. Eng.* **2018**, *51*, 1−8.
(37) Vasileiadis, M.; Peristeras, L. D.; Papavasileiou, K. D.; Economou, I. G. Modeling of bulk kerogen porosity: Methods for control and characterization. *Energy Fuels* **2017**, *31*, 6004−6018.
(38) Wang, Z.; Li, Y.; Liu, H.; Zeng, F.; Guo, P.; Jiang, W. Study on the adsorption, diffusion and permeation selectivity of shale gas in organics. *Energies* **2017**, *10*, 142.
(39) Zhao, T.; Li, X.; Zhao, H.; Li, M. Molecular simulation of adsorption and thermodynamic properties on type II kerogen: Influence of maturity and moisture content. *Fuel* **2017**, *190*, 198−207.
(40) Zhao, T.; Li, X.; Ning, Z.; Zhao, H.; Li, M. Molecular simulation of methane adsorption on type II kerogen with the impact of water content. *J. Pet. Sci. Eng.* **2018**, *161*, 302−310.
(41) Ho, T. A.; Wang, Y.; Criscenti, L. J. Chemo-mechanical coupling in kerogen gas adsorption/desorption. *Phys. Chem. Chem. Phys.* **2018**, *20*, 12390−12395.
(42) Huang, L.; Ning, Z.; Wang, Q.; Qi, R.; Zeng, Y.; Qin, H.; Ye, H.; Zhang, W. Molecular simulation of adsorption behaviors of methane, carbon dioxide and their mixtures on kerogen: Effect of kerogen maturity and moisture content. *Fuel* **2018**, *211*, 159−172.
(43) Obliger, A.; Ulm, F.-J.; Pellenq, R. J.-M. Impact of nanoporosity on hydrocarbon transport in shales' organic matter. *Nano Lett.* **2018**, *18*, 832−837.
(44) Vasileiadis, M.; Peristeras, L. D.; Papavasileiou, K. D.; Economou, I. G. Transport properties of shale gas in relation to kerogen porosity. *J. Phys. Chem. C* **2018**, *122*, 6166−6177.
(45) Collell, J.; Galliero, G.; Gouth, F.; Montel, F.; Pujol, M.; Ungerer, P.; Yiannourakou, M. Molecular simulation and modelisation of methane/ethane mixtures adsorption onto a microporous molecular model of kerogen under typical reservoir conditions. *Microporous Mesoporous Mater.* **2014**, *197*, 194−203.
(46) Zhou, B.; Xu, R.; Jiang, P. Novel molecular simulation process design of adsorption in realistic shale kerogen spherical pores. *Fuel* **2016**, *180*, 718−726.
(47) Collell, J.; Ungerer, P.; Galliero, G.; Yiannourakou, M.; Montel, F.; Pujol, M. Molecular simulation of bulk organic matter in type II shales in the middle of the oil formation window. *Energy Fuels* **2014**, *28*, 7457−7466.
(48) Firouzi, M.; Wilcox, J. Molecular modeling of carbon dioxide transport and storage in porous carbon-based materials. *Microporous Mesoporous Mater.* **2012**, *158*, 195−203.
(49) Firouzi, M.; Wilcox, J. Slippage and viscosity predictions in carbon micropores and their influence on $CO_2$ and $CH_4$ transport. *J. Chem. Phys.* **2013**, *138*, 064705.
(50) Wu, H.; Chen, J.; Liu, H. Molecular dynamics simulations about adsorption and displacement of methane in carbon nanochannels. *J. Phys. Chem. C* **2015**, *119*, 13652−13657.
(51) Jin, Z.; Firoozabadi, A. Flow of methane in shale nanopores at low and high pressure by molecular dynamics simulations. *J. Chem. Phys.* **2015**, *143*, 104315.
(52) Jin, Z.; Firoozabadi, A. Phase behavior and flow in shale nanopores from molecular simulations. *Fluid Phase Equilib.* **2016**, *430*, 156−168.
(53) Sun, H.; Zhao, H.; Qi, N.; Li, Y. Molecular insights into the enhanced shale gas recovery by carbon dioxide in kerogen slit nanopores. *J. Phys. Chem. C* **2017**, *121*, 10233−10241.
(54) Zhang, L.; Li, J.; Jia, D.; Zhao, Y.; Xie, C.; Tao, Z. Study on the adsorption phhenomenon in shale with the combination of molecular dynamic simulation and fractal analysis. *Fractals* **2018**, *26*, 1840004.
(55) Okamoto, N.; Kobayashi, K.; Liang, Y.; Murata, S.; Matsuoka, T.; Akai, T.; Takagi, S. Slip velocity of methane flow in nanopores with kerogen and quartz surfaces. *SPE J.* **2017**, *23*, 102−116.
(56) Bharati, S.; Patience, R. L.; Larter, S. R.; Standen, G.; Poplett, I. J. F. Elucidation of the alum shale kerogen structure using a multi-disciplinary approach. *Org. Geochem.* **1995**, *23*, 1043−1058.
(57) Vandenbroucke, M. Kerogen: From types to models of chemical structure. *Oil Gas Sci. Technol.* **2003**, *58*, 243−269.
(58) Kondla, D.; Sanei, H.; Clarkson, C. R.; Ardakani, O. H.; Wang, X.; Jiang, C. Effects of organic and mineral matter on reservoir quality in a middle triassic mudstone in the canadian arctic. *Int. J. Coal Geol.* **2016**, *153*, 112−126.
(59) Kelemen, S. R.; Afeworki, M.; Gorbaty, M. L.; Sansone, M.; Kwiatek, P. J.; Walters, C. C.; Freund, H.; Siskin; Bence, A. E.; Curry, D. J.; et al. Direct characterization of kerogen by X-ray and solid-state $^{13}C$ nuclear magnetic resonance methods. *Energy Fuels* **2007**, *21*, 1548−1561.
(60) Zou, C. *Unconventional petroleum geology*; Elsevier, 2017.
(61) Zhao, H.; Lai, Z.; Firoozabadi, A. Sorption hysteresis of light hydrocarbons and carbon dioxide in shale and kerogen. *Sci. Rep.* **2017**, *7*, 16209.
(62) Plimpton, S. Fast parallel algorithms for short-range molecular dynamics. *J. Comput. Phys.* **1995**, *117*, 1−19.
(63) Nosé, S. A unified formulation of the constant temperature molecular. *J. Chem. Phys.* **1984**, *81*, 511−519.
(64) Nosé, S. A molecular dynamics method for simulations in the canonical ensemble. *Mol. Phys.* **1984**, *52*, 255−268.
(65) Nosé, S.; Klein, M. L. A study of solid and liquid carbon tetrafluoride using the constant pressure molecular dynamics technique. *J. Chem. Phys.* **1983**, *78*, 6928−6939.


DOI: 10.1021/acs.jpcc.8b07123
*J. Phys. Chem. C* 2018, 122, 23528−23542

(66) Hoover, W. G. Constant-pressure equations of motion. *Phys. Rev. A: At., Mol., Opt. Phys.* **1986**, *34*, 2499−2500.
(67) Sun, H.; Mumby, S. J.; Maple, J. R.; Hagler, A. T. An ab initio CFF93 all-atom force field for polycarbonates. *J. Am. Chem. Soc.* **1994**, *116*, 2978−2987.
(68) Sun, H. Ab initio calculations and force field development for computer simulation of polysilanes. *Macromolecules* **1995**, *28*, 701−712.
(69) Yiannourakou, M.; Ungerer, P.; Leblanc, B.; Rozanska, X.; Saxe, P.; Vidal-Gilbert, S.; Gouth, F.; Montel, F. Molecular simulation of adsorption in microporous materials. *Oil Gas Sci. Technol.* **2013**, *68*, 977−994.
(70) Materials Design S.A.R.L. http://www.materialsdesign.com/ (accessed May 1, 2017).
(71) Waldman, M.; Hagler, A. T. New combining rules for rare gas van der waals parameters. *J. Comput. Chem.* **1993**, *14*, 1077−1084.
(72) Chempath, S.; Clark, L. A.; Snurr, R. Q. Two general methods for grand canonical ensemble simulation of molecules with internal flexibility. *J. Chem. Phys.* **2003**, *118*, 7635−7643.
(73) Herrera, L.; Do, D. D.; Nicholson, D. A monte carlo integration method to determine accessible volume, accessible surface area and its fractal dimension. *J. Colloid Interface Sci.* **2010**, *348*, 529−536.
(74) Düren, T.; Millange, F.; Férey, G.; Walton, K. S.; Snurr, R. Q. Calculating geometric surface areas as a characterization tool for metal-organic frameworks. *J. Phys. Chem. C* **2007**, *111*, 15350−15356.
(75) Bhattacharya, S.; Gubbins, K. E. Fast method for computing pore size distributions of model materials. *Langmuir* **2006**, *22*, 7726−7731.
(76) Tesson, S. Un champ de force polarisable pour l'étude des argiles à l'échelle moléculaire. *Ph.D. thesis*, Université Pierre et Marie Curie-Paris VI, 2016.
(77) Frenkel, D.; Smit, B. *Understanding molecular simulation: From algorithms to applications*; Academic Press, 2001; Vol. *1*.
(78) Zhou, L.; Sun, Y.; Zhou, Y. An experimental study on the adsorption behavior of gases crossing the critical temperature. *Chin. J. Chem. Eng.* **2002**, *10*, 259−262.
(79) Cygan, R. T.; Guggenheim, S.; Koster van Groos, A. F. Molecular models for the intercalation of methane hydrate complexes in montmorillonite clay. *J. Phys. Chem. B* **2004**, *108*, 15141−15149.
(80) Jin, Z.; Firoozabadi, A. Methane and carbon dioxide adsorption in clay-like slit pores by monte carlo simulations. *Fluid Phase Equilib.* **2013**, *360*, 456−465.
(81) Jin, Z.; Firoozabadi, A. Effect of water on methane and carbon dioxide sorption in clay minerals by monte carlo simulations. *Fluid Phase Equilib.* **2014**, *382*, 10−20.
(82) Psarras, P.; Holmes, R.; Vishal, V.; Wilcox, J. Methane and $CO_2$ adsorption capacities of kerogen in the eagle ford shale from molecular simulation. *Acc. Chem. Res.* **2017**, *50*, 1818−1828.
(83) Billemont, P.; Coasne, B.; De Weireld, G. Adsorption of carbon dioxide, methane, and their mixtures in porous carbons: effect of surface chemistry, water content, and pore disorder. *Langmuir* **2013**, *29*, 3328−3338.


DOI: 10.1021/acs.jpcc.8b07123
*J. Phys. Chem. C* 2018, 122, 23528−23542